Eur. Phys. J. B
https://doi.org/10.1140/epjb/s10051-020-00027-1

THE EUROPEAN
PHYSICAL JOURNAL B

Regular Article - Solid State and Materials

Magnetic-field induced multi-step transitions in ferromagnetic spin-crossover solids within the BEG model

T. D. Oke[1,2,a], M. Ndiaye[2], F. Hontinfinde[1], and K. Boukheddaden[2]

[1] Département de Physique (FAST) et Institut des Mathématiques et de Sciences Physiques (IMSP), Université d'Abomey-Calavi, 01, BP 613, Porto-Novo, Benin
[2] Groupe d'Etudes de la Matière Condensée, Université Paris-Saclay, Université de Versailles/St. Quentin en Yvelines-CNRS, 45 Avenue des Etats Unis., 78035 Versailles Cedex, France

Received 12 August 2020 / Accepted 23 November 2020

Abstract. We study by means of the 2D Blume–Emery–Griffiths (BEG) spin-1 model, spin-crossover (SCO) and prussian blue analogs (PBAs) solids. In this model, the spin states, which can be high-spin (HS) or low-spin (LS), interact magnetically and elastically with their nearest neighbors. To account for the volume change, accompanying the spin transition phenomenon, all interactions through the lattice are assumed as temperature-dependent. In addition, the system is subject to a variable magnetic field lifting the degeneracy in the HS state. A stochastic cooperative dynamics of this BEG-like Hamiltonian, describing the equilibrium and nonequilibrium properties of ferromagnetic spin-crossover solids, is derived from the Glauber approach, with appropriate Arrhenius microscopic transition rates. The model generates under the magnetic field, sigmoidal relaxation and a hysteresis phenomenon of the HS fraction, as well as multistep behavior of the magnetization. These behaviors open the way to new route of multi-stable systems, desired in multi-byte electronics.

1 Introduction

Spin-crossover (SCO) materials [1–5] are potential promising compounds used in technologies for the design of miniaturized devices with fast response, in the field of the treatment and storage of informations. A variety of compounds with $4 \sim 7$ d-electrons, usually exhibits a bistability with high-spin (HS) and low-spin (LS) configurations due to the competition between the Pauli exclusion principle and the crystal field energy. Such materials can undergo transitions under various stimuli such as, emitting light, variations of temperature or pressure, generating magnetic and electric fields, etc., [6–12]. Usually, thermally-induced spin transitions in SCO materials lead to both electric and structural changes, often observed as a color and global magnetization changes [1,13,14]. During these events, the HS fraction undergoes a smooth change when the temperature is increased in the presence of weak interactions between SCO units. When these interactions become strong, first-order transitions appear [15–17], followed by a large thermal hysteresis. An usually cited example that exhibits such transition near the room temperature, is that of the $[Fe(NH_2trz)_3](NO_3)_2, (NH_2trz = 4-amino-1,2,4-triazole)$ [18]. In solid state, the SCO transition takes place by changes of unit-cell volume and bond length which are considerably larger in the HS state. Beyond the larger electronic degeneracy which emerges, a larger phonon density for the HS state is also obtained [15,16,19]. In the case of $Fe(II)$, the SCO phenomenon results from the redistribution of the electrons between the bonding t_{2g} and the antibonding e_g orbitals. Several experimental investigations allow to estabilish that SCO transitions involve both electronic transformation (spin and orbital) and structural modifications [20–25] which are governed by the elastic interactions [26–31,33–45].

The spin transition processes have been addressed within Ising-like models where the cooperativity between Ising spins is described by exchange interactions [46,47]. Most of physical properties observed in SCO systems have been reproduced. In particular, the two-step thermal spin-transition in mononuclear systems by means of two interacting sublattices within the mean-field approximation [46,48]. It has also been studied with short and long range interactions using an exact approach for low-dimensional systems [27]. Beyond that, Boukheddaden et al. [28,29] have studied an Ising-like model of SCO solids with static and dynamic effects of light within the mean-field approach where their multi-stability characters have been pointed out. Very recently, Pavlik et al. [49] used coupled magnetic interactions and an Ising-like model to describe

---

[a] e-mail: oketous3@gmail.com (corresponding author)

magnetically-coupled binuclear compounds leading to obtain bistable and tristable thermal spin transitions.

In the present investigations, we consider a SCO system containing both elastic and magnetic interactions between the SCO sites for which we study the thermal properties under a static magnetic field. The Blume–Emery–Griffiths (BEG) Hamiltonian allows to account for both type of interactions through the quadrupolar and exchange interactions. The choice of the BEG model is also dictated by the existence of a rich literature on spin models applied to crossover solids [50–62]. In previous works [63–65], the quadrupolar coupling parameter, K, between the SCO units was assumed to depend linearly on the absolute temperature T in the form, $K = \alpha k_B T$ in order to mimic the elastic interactions. On the other hand, the effective "ligand-field" energy, D, depends on the absolute temperature and contains the combined effects of the ligand field strength and that the degeneracy ratio between LS and HS states which results in an entropic term. We solved the problem of the BEG Hamiltonian, combining "elastic" and magnetic interactions as well as effective ligand-field energy and static magnetic field looking for both nonequilibrium and equilibrium properties in the mean-field approximation. The nonequilibrium properties have been derived from the resolution of the master equation in which Glauber dynamics is used for the magnetic spin-flip while Arrhenius rates are considered for the transitions between the low-spin and the high-spin states [64–67]. As a result, two nonlinear and coupled differential equations of motion on the total magnetization, m and high-spin fraction, n_{HS}, are obtained whose stationary state allow obtaining the equilibrium properties of the system. The multi-step transitions appear when the magnetic-field is swept in isothermal conditions at a temperature located at the vicinity of thermal hysteresis loops.

The paper is organized as follows. Section 2 contains the presentation of the BEG model used for SCO systems and the description of the calculation method . In Sect. 3, we present and discuss the obtained results, and in Sect. 4, we conclude and outline some possible extensions of this work.

2 The model Hamiltonian

The BEG model spin-1 Hamiltonian, adapted for SCO materials with elastic and magnetic interactions and including an applied magnetic field, writes as follows [31,32]:

$$H = -J \sum_{\langle i,j \rangle} \sigma_i \sigma_j - K \sum_{\langle i,j \rangle} \sigma_i^2 \sigma_j^2 + D \sum_i \sigma_i^2 - h \sum_i \sigma_i \tag{1}$$

where $\sigma_i = \pm 1, 0$ are the fictitious spin values located at site i of the square lattice. The spins $\sigma_i = \pm 1$ describe the magnetic HS spin state and $\sigma_i = 0$ is associated with the diamagnetic LS state. As in Ref. [68], only nearest-neighbor (nn) interactions are considered. The magnetic interactions between the magnetic states, $\sigma_i = \pm 1$, are taken into account through the exchange term J and the quadrupolar interactions (between the SCO sites) are introduced through the parameter, K, with $J/K = \gamma$. Due to the elastic nature of the SCO transition [59–62,69], the K- term takes into account the phonon contribution, originating from both intra- and inter-molecular vibrations. In fact, the volume change accompanying the spin transition of each molecule, delocalizes the strain field, through acoustic phonons and lattice distortions, everywhere in the lattice, which provides the elastic long-range character of the interactions between the SCO units. Hence, the quadrupolar term, which depends on the average value of the quadratic displacement at each site, is then written as follows, $K = \alpha k_B T$ [63–65]. In the one site contribution, $D\sigma_i^2$, the parameter, $D = \Delta - k_B T \ln(g)$, accounts for the effective ligand field energy, which contains the 0 K energy gap, Δ, and the entropy contribution, $k_B T \ln(g)$, arising from the difference of electro-vibrational degeneracies of HS and LS states, which have different spin states and different elastic moduli. In the last contribution, $h\sigma_i$, h is the energetic contribution of the external magnetic field. The ligand-field strength between LS and HS states is set to $400K$.

2.1 Mean-field theory (MFT) approach

In mean-field theory, the total Hamiltonian writes as a sum of one site contributions, where each spin located at site, i, feels the following one-site Hamiltonian, H_i [68]:

$$H_i(\sigma_i) = -zJm\sigma_i - zKn_{HS}\sigma_i^2 + D\sigma_i^2 - h\sigma_i \tag{2}$$

where $m = \langle \sigma_i \rangle$ and $n_{HS} = \langle \sigma_i^2 \rangle$ are considered as invariant by translation over the lattice.

Following [68], the mean-field free energy per site is given by:

$$F(m, n_{HS}, T) = E - TS_{ent}, \tag{3}$$

where E and S_{ent} are the internal energy and entropy per site of the system, respectively given by:

$$E = -\frac{z}{2}Jm^2 - \frac{z}{2}Kn_{HS}^2 + Dn_{HS} - hm; \tag{4}$$

$$S_{ent} = k_B \beta \langle H_i \rangle + k_B \ln \sum_{\sigma_i} e^{-\beta H_i}. \tag{5}$$

Here, $\beta = \frac{1}{k_B T}$ (T is the absolute temperature and k_B is the Boltzmann constant) and $\langle H_i \rangle = -zJm^2 - zKn_{HS}^2 + Dn_{HS} - hm$ is the average value of H_i. After some simple calculations, the variational free energy is given by:

$$F(m, n_{HS}, T) = \frac{z}{2}Jm^2 + \frac{z}{2}Kn_{HS}^2 \\ -k_B T \ln\left[1 + 2e^{\beta(zKn_{HS}-D)}\cosh\beta(zJm+h)\right]. \tag{6}$$

2.2 Dynamic choice and equations of motion

The physical properties of Hamiltonian (1) are investigated in the frame of microscopic master equation which governs the time evolution of the probability $P(\{\sigma_i\}, t)$ to occupy the spin configuration $\{\sigma\}$ at time t [45,64–67]. The expression of the flux of probability, $\frac{\partial P(\{\sigma\},t)}{\partial t}$ accounting for stochastic transitions between the electronic configurations $\{\sigma\}_i \rightleftarrows \{\sigma'\}_i$ with transition rates W, due to the interaction with the thermal bath, writes in the frame of the Glauber dynamics as follows:

$$\frac{\partial P(\{\sigma\},t)}{\partial t} = -\sum_{i=1}^{N} W_i(\sigma_i \to \sigma_i')P(\{\sigma_i\},t) \\ + \sum_{i=1}^{N} W_i(\sigma_i' \to \sigma_i)P(\{\sigma_i'\},t), \tag{7}$$

where $W_i(\sigma_i \to \sigma_i')$ is the transition rate of spin state σ_i from the value σ_i to σ_i'. To fulfill the specific Arrhenius spin flip of SCO sites, the expression of $W_i(\sigma_i \to \sigma_i')$ is written under the following form:

$$W_i(\sigma_i \to \sigma_i') = \frac{1}{3\tau}\frac{e^{-\beta H_i(\sigma_i')}}{\sum_{\sigma_i} e^{-\beta H_i(\sigma_i)}}, \tag{8}$$

where, $\frac{1}{\tau}$ denotes the effective intramolecular frequency associated with the "spontaneous spin reversal" [64–67] :

$$\frac{1}{\tau} = \frac{1}{\tau_0}e^{-\beta E_0^a}, \tag{9}$$

in which $1/\tau_0$ represents the "intrinsic" molecular frequency of the spin-flip process between HS and LS states, taken as constant and E_0^a denotes the intramolecular vibronic energy barrier, which originates form the deformation of the molecule subsequent to the spin state change [70].

In the equilibrium state, the probabilities satisfy the following detailed balance condition:

$$\frac{W(\sigma_i \to \sigma_i')}{W(\sigma_i' \to \sigma_i)} = \frac{P_{eq}(\{\sigma\}_i, \sigma_i')}{P_{eq}(\{\sigma\}_i, \sigma_i)}, \tag{10}$$

where, $P_{eq}(\{\sigma\}_i, \sigma_i')$ is the Boltzmann probability to occupy the lattice site i by σ_i'. The used expressions of the transition rates, respecting the previous detailed balance, are:

$$W_i(\sigma_i \to \sigma_i') = W_i(\sigma_i') \\ = \frac{1}{3\tau}\frac{e^{-\beta H_i(\sigma_i')}}{1 + 2e^{\beta(zKn_{HS}-D)}\cosh\beta(zJm+h)}. \tag{11}$$

The time dependence of the average values of the two relevant spin operators, σ_k, and σ_k^2, respectively associated to the magnetization, $m = \langle\sigma\rangle$ and HS fraction, $n_{HS} = \langle\sigma^2\rangle$, are calculated as follows:

$$m = \sum_{\{\sigma\}} \sigma_k P(\{\sigma_k\},t) \quad \text{and} \quad n_{HS} = \sum_{\{\sigma\}} \sigma_k^2 P(\{\sigma_k\},t). \tag{12}$$

Using, the expression of the master equation (7) combined with those of the transition probabilities (11) and Eq. (12), one can arrive after some calculations, to the following analytical coupled differential equations of motion of the magnetization m and the fraction n_{HS},

$$\begin{cases} \frac{dm}{dt} = \frac{e^{-\beta E_0^a}}{3\tau_0}\left(-m + \frac{2\sinh\beta(zJm+h)}{e^{-\beta(zKn_{HS}-D)}+2\cosh\beta(zJm+h)}\right) \\ \frac{dn_{HS}}{dt} = \frac{e^{-\beta E_0^a}}{3\tau_0}\left(-n_{HS} + \frac{2\cosh\beta(zJm+h)}{e^{-\beta(zKn_{HS}-D)}+2\cosh\beta(zJm+h)}\right) \end{cases}. \tag{13}$$

Equations of motion (13) are solved numerically using the well-know Runge–Kutta method. Both equilibrium and dynamical properties of the system will be analyzed below as a function of temperature and magnetic field energy, h.

3 Results and discussions

This section is devoted to the presentation of the thermodynamic properties of the ferromagnetic SCO system under magnetic field form the point of view of their equilibrium and non-equilibrium properties.

3.1 Equilibrium properties of the system under a static magnetic-field

3.1.1 Thermal equilibrium properties in the zero applied magnetic-field case

First, we analyze the equilibrium case ($\frac{\partial m}{\partial t} = 0$ and $\frac{\partial n_{HS}}{\partial t} = 0$). The coupled self-consistent equations of state of the system are given by Eq. (14), describing the thermal dependence of the HS fraction and magnetization in the framework of the mean-field theory (MFT) in the presence of external magnetic field.

$$\begin{cases} m = \frac{2\sinh\beta(zJm+h)}{e^{-\beta(zKn_{HS}-D)}+2\cosh\beta(zJm+h)} \\ n_{HS} = \frac{2\cosh\beta(zJm+h)}{e^{-\beta(zKn_{HS}-D)}+2\cosh\beta(zJm+h)}. \end{cases} \tag{14}$$

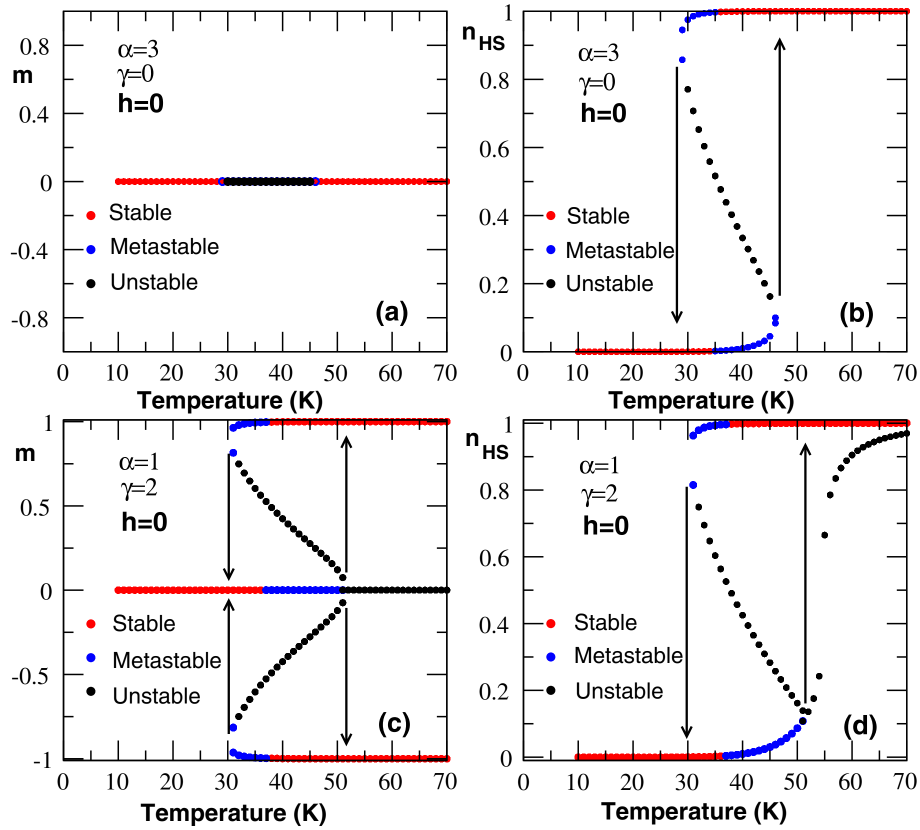

Fig. 1 Thermal behavior of magnetization m and n_{HS} fraction in the absence of magnetic-field energy ($h = 0$). First-order spin-transition is obtained with sigmoidal shapes in their behaviors for selected values of α and γ. **a**, **b** are obtained for $\alpha = 3$ and $\gamma = 0$. There, $m = 0$ whereas n_{HS} fraction raises from LS to HS state through intermediate states. In **c**, **d**, different states are depicted through m and n_{HS} behaviors for $\alpha = 1$ and $\gamma = 2$. Different color codes, red, blue and black are used here to identify stable, metastable and unstable states, respectively

In this section, the magnetic field energy is set to zero. Equations (14) are solved using the Newton-Raphson method in the interval 10-70 K with temperature step $\Delta T = 1.$ K. The obtained results are summarized in Fig. 1 for selected values of model parameters.

Figure 1a, b display the thermal behaviors of the magnetization m and the fraction n_{HS} for $\alpha = 3$ and $\gamma = 0$ ($\alpha = K/k_BT$, $\gamma = J/K$), then without any magnetic coupling. The spin transition that appeared on n_{HS} is of first-order as obtained in Ref. [68], while the magnetic system stays diamagnetic ($<\sigma>= 0$ and $<\sigma^2>= 0$) in the LS state and becomes paramagnetic ($<\sigma>= 0$ and $<\sigma^2>= 1$) in the HS state, thus keeping always the value $m = 0$.

When the magnetic coupling becomes nonzero, as in the case of Fig. 1c, d ($\gamma = 2$, $\alpha = 1$), $m = 0$ is still a trivial solution at all temperatures (see Eq. (14) but new solutions appear in the thermal dependence of n_{HS} and nonzero solutions exist for $m(T)$, which shows now a thermally-induced magnetic first-order transition.

3.1.2 Magnetic-field induced multi-step transitions with $J = 0$

We now investigate, in isothermal conditions, the effect of the applied magnetic field energy, h, on the stability of the HS and LS states. At this end, the system's properties are studied for varying h parameter in the interval -200 and 200 K, which allows to visit all possible configurations of the system, where the biquadratic contribution, K (corresponding to phonons effect) is kept nonzero. In the absence of magnetic interactions, ($\gamma = 0$) corresponding to the thermal dependence of magnetization and HS fraction depicted in Fig. 1a, b, respectively, the application of a magnetic field, h, generates interesting model properties, as shown in Fig. 2.

We first look to the system properties at three selected temperatures: $T = 30$; 35; 50 K and varying magnetic field energy h (Fig. 2). It was observed in Fig. 1a, b that at $T = 30$ K and $h = 0$ the system could be in the stable, metastable or unstable state characterized by values of the average magnetization (m) and the HS fraction (n_{HS}). For $m = 0$ and $n_{HS} = 0$, the system lays in a pure diamagnetic phase. Figure 2a, b clearly reproduce the previous findings and show three solutions for m and n_{HS} at $h = 0$. The HS fraction displays a stable solution at $n_{HS} = 0$, a metastable solution around $n_{HS} \simeq 1$ and an unstable one at $n_{HS} \simeq 2/3$. The latter denotes a configuration constituted by a diagmagnetic and a paramagnetic phases. For $T = 35K$ and $h = 0$, a very similar situation with the previous one is obtained (Fig. 2c, d) while at $T = 50K$, where

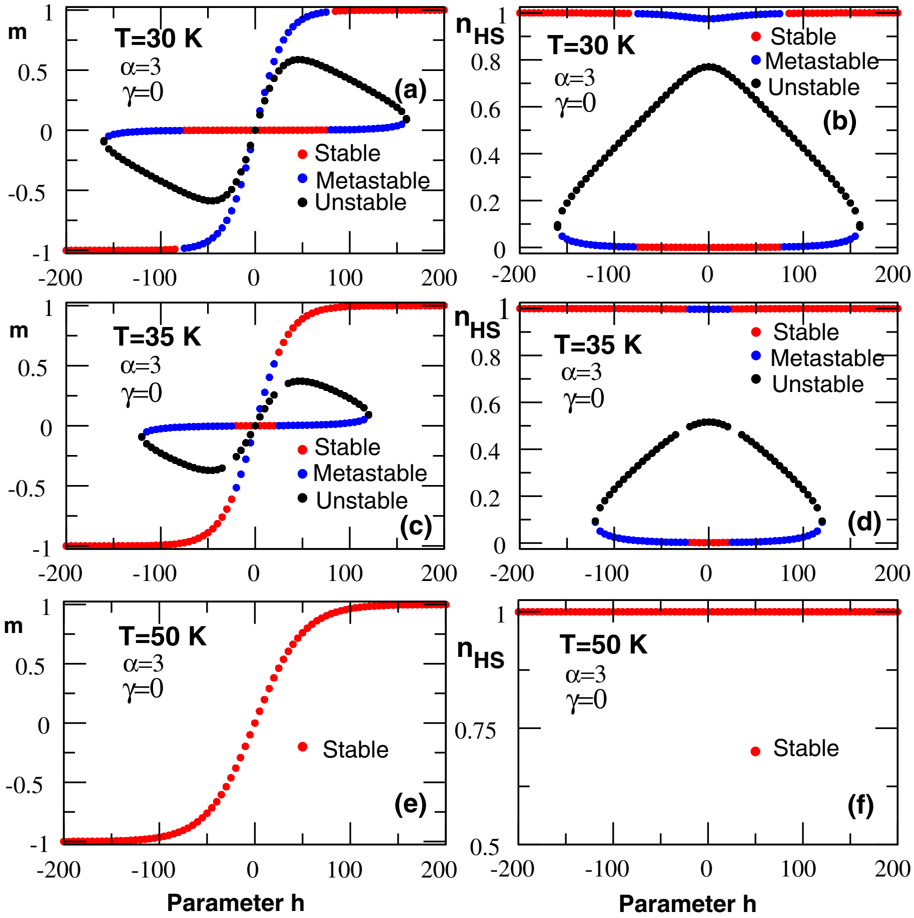

Fig. 2 Multi-spin states transition of magnetization m and n_{HS} fraction with varying magnetic-field energy for $\gamma = 0$ and $\alpha = 3$. For low temperatures, intermediate spin states are got in the absence of magnetic interactions, whereas these are disappeared at high temperature (see text). The color code, red, blue and black is used here to identify the stable, metastable and unstable states, respectively

the system is fully HS, a paramagnetic phase ($m = 0$; $n_{HS} = 1$) is got for $h = 0$.

Interestingly for $T = 30$ K, the magnetic field effect leads to "butterfly" curve for the magnetization versus h and to a typical $n_{HS}(h)$ curve containing hidden states. Indeed, $T = 30$ K is very close to the spinodal point, that is the limit of metastability in the curve $n_{HS}(T)$ of Fig. 1a, b. If we start the simulations with $h = 0$, the magnetization has only stable solution, $m = 0$, while the HS fraction possesses three solutions, $n_{HS} = 0$, $n_{HS} = 0.77$ and 0.97. Here, $n_{HS} = 0.97$ is the metastable solution, $n_{HS} = 0.77$ is unstable and $n_{HS} = 0$ is the stable one. Increasing the field h, which acts exclusively on the HS species ($\sigma_i = \pm 1$), stabilizes the HS state at expenses of the LS state. As a result, the metastable line state $n_{HS} = 0$ evolves to as to join the unstable curve, for the value of the "critical field energy" $h_c = 155$ K, leading to form the closed loop appearing in Fig. 2b. This closed loop leads to the "butterfly" curve obtained in Fig. 2a, where the horizontal part corresponds to the evolution under field of the diamagnetic metastable solution $n_{HS} = 0$ (Fig. 2b), which joins the unstable branch at turning points A and B, corresponding to the respective switching or spinodal magnetic field values $h_- \simeq -160$ and $h_+ \simeq 160$. On the other hand this butterfly loop is limited along the magnetization axis by the extreme values $m \simeq -0.6$ and $m \simeq +0.6$. Finally, the continuous line (in tangent hyperbolic shape) giving the gradual transition on the magnetization switching under field between $m = -1$ and $m = +1$ in Fig. 2a corresponds to the top solution $n_{HS}(h)$ of Fig. 2b. The latter shows that only few diamagnetic species appear around the region $h = 0$ and so the system remains almost paramagnetic in this state. Figure 2c, d, calculated at $T = 35$ K show the system behavior under magnetic field inside the bistable region of the thermal hysteresis of Fig. 1a, b. Surprisingly very similar behaviors to those of Fig. 2a, b are obtained, although the butterfly loop shows for this case lower limiting values for the magnetization and the spinodal magnetic fields ($m \simeq -0.37$ and $m \simeq +0.37$ and $h_- \simeq -120$ and $h_+ \simeq 120$). In contrast, very similar gradual continuous curve $m(h)$ is obtained in Fig. 2a, c. This similarity can be well understood by comparing the corresponding $n_{HS}(h)$ curves of Fig. 2d, b. We remark that in Fig. 2d, the solution $n_{HS}(h) = 1$ holds at all temperatures, which means that system remains purely HS and paramagnetic along the grad-

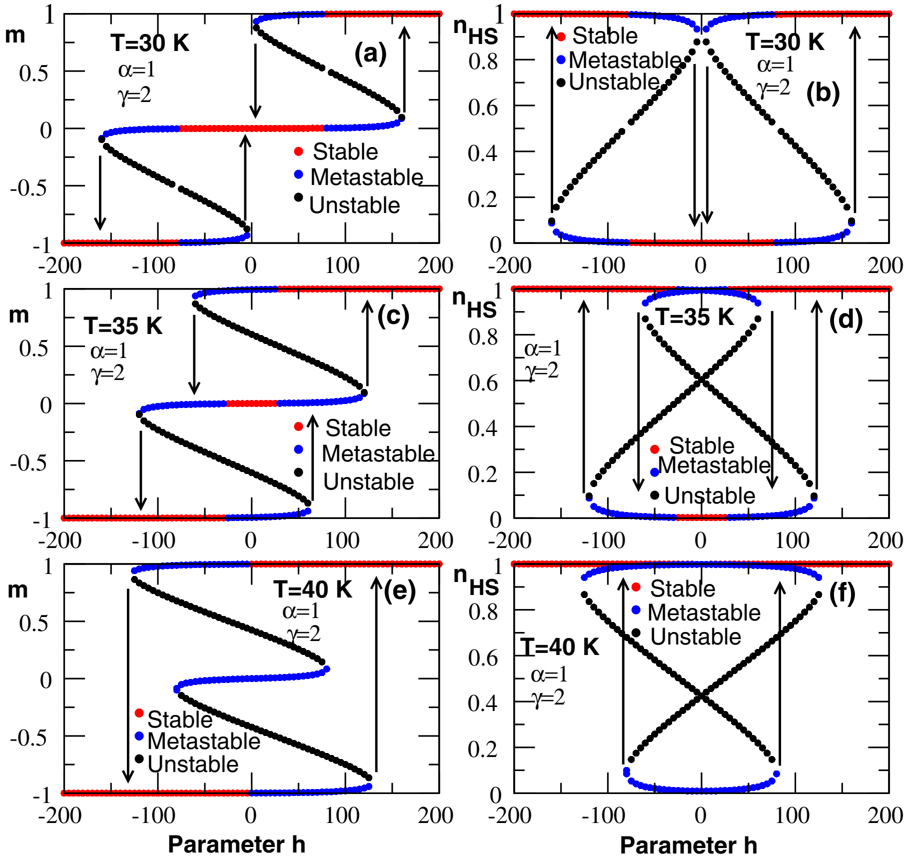

Fig. 3 Effect of the magnetic-field energy on the spin-transition in the vicinity and inside the thermal hysteresis loops of Fig. 1 for $\alpha = 1$ and $\gamma = 2$. The behaviors of magnetization m and n_{HS} fraction are depicted through all panels at fixed temperature. The upper and lower switching fields at the border of the loops, respectively h_1^+,h_1^-) for the negative magnetization part and (h_2^+; h_2^- for the positive one, are temperature-dependent quantities. Different phases are shown in Fig. 5. Stable (S), Unstable (U) and Metastable (M) states are obtained

ual transition. For $T = 50$ K, the SCO system is HS (paramagnetic) according to Fig. 1. So, the application of the magnetic field (see Fig. 2e, f) does not induce any metastability in the system, which converts form the ordered HS state with $m = -1$ to the other with $m = +1$ and where the HS fraction n_{HS} remains equal to 1 at all temperatures. It is interesting to comment on the symmetry of the obtained solution $m(h)$ and $n_{HS}(h)$. Indeed, the magnetization clearly fulfill the relation $m(-h) = -m(h)$, it is then anti-symmetric, which is always true whatever the temperature and the parameter values, while the HS fraction is clearly symmetric with respect of the inversion of the field, $n_{HS}(-h) = n_{HS}(h)$. These properties are very general and originate from the expressions of the self-consistent equations (14), which remain invariant when we change the triplet m, n_{HS}, h by $-m, n_{HS}, -h$. It is worth to mention the importance of the preparation of the initial state and its effect on the obtained curve $m(h)$ and $n_{HS}(h)$. Let us take the case of Fig. 2a, b corresponding to the hysteresis of Fig. 1a for $T = 30$ K. If we start in Fig. 2a initially for $h = 0$ from the diamagnetic state ($m = 0$ and $n_{HS} = 0$), decreasing or increasing the field h will lead the system to reach, in a first-order fashion, the paramagnetic state $n_{HS}(h) \simeq 1$. Whatever, the initial state, the system will always reach the stable line $n_{HS}(h) \simeq 1$, where it will stay definitely.

When varying the magnetic field energy sequentially from -160 K to 160 K, around $h = 0$ K, where the corresponding magnetization is $m = 0$, all solutions are between -1 and $+1$ states. A symmetric curve is obtained and centered on zero and three solutions are got on both sides. The n_{HS} fraction shows the typical behaviors but at zero field, three states are depicted. The first one is the LS state, the second is the HS state and the third which is the intermediate state stands between them as LS-HS states. At $T = 35$ K, similar results are obtained but the intermediate states are reduced in number (see Fig. 2c, d).

These phenomena are temperature-dependent and intermediate spin states disappear at high temperature (see Fig. 2e, f).

3.1.3 Magnetic-field induced multi-step transitions with magnetic interactions and hysteresis phenomena

In Fig. 3, we analyzed the behaviors of the magnetization, m, and the HS fraction, n_{HS}, under variable magnetic-field at fixed temperature in the presence of

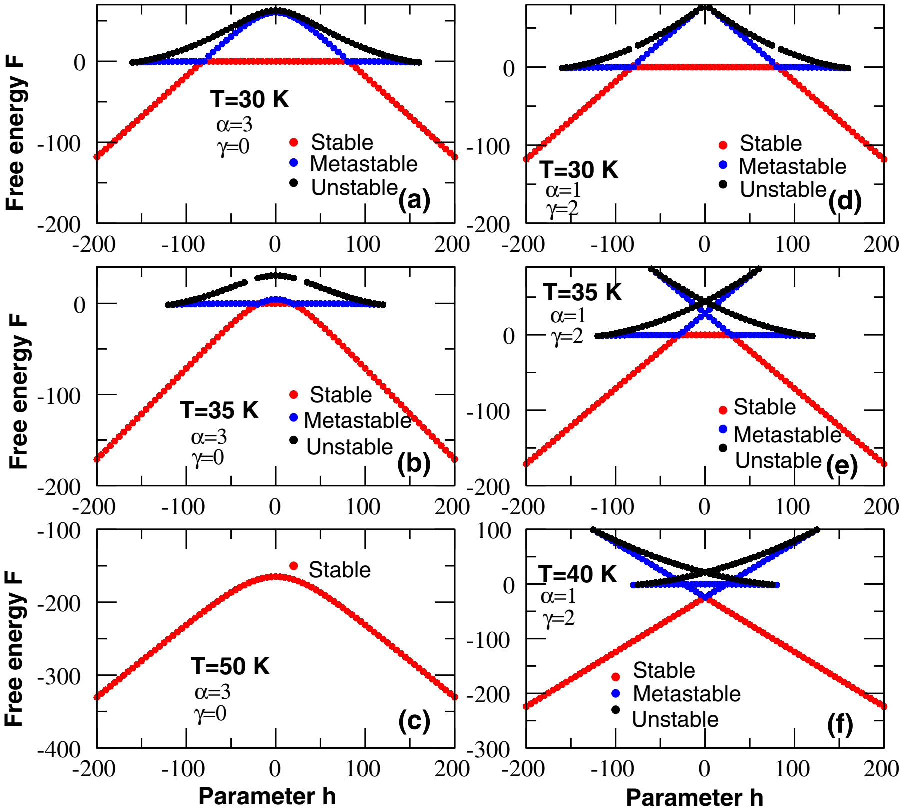

Fig. 4 Free energy F as function of magnetic-field parameter at different temperatures and model parameter values, showing the stability of the obtained solutions in Figs. 2 and 3. Red, blue and black lines correspond to stable (S), metastable (M) and unstable (U) solutions, respectively. For $\alpha = 3$ and $\gamma = 0$ (left panels), stable states take place for increasing temperature, **a** $T = 30$ K, **b** $T = 35$ K and **c** $T = 50$ K. For the parameters values, $\alpha = 1$ and $\gamma = 2$ (right panels) and **d** $T = 30$ K, **e** $T = 35$ K and **f** $T = 40$ K, the free energy shows horns features characteristic of the existence of hysteresis intricate unstable phases

magnetic ($\gamma = 2$) and phonons ($\alpha = 1$) interactions. Different macroscopic states are got and their number increases with the temperature T.

When magnetic interactions are introduced (Fig. 1c, d), thermal first-order transitions are got on both physical parameters, $m(T)$ and $n_{HS}(T)$. Let us consider the similar study under field as for the case of Fig. 1a, b in the three regions, where the self-consistent equations of state (14) admit one stable solutions (from both sides of the thermal hysteresis) or three [stable (S), metastable (M) and unstable (U)] solutions inside the thermal hysteresis. There, the unstable states are characterized with negative slopes ($\frac{dm}{dh} < 0$ or $\frac{dn_{HS}}{dh} < 0$). The application of the magnetic field, in the LS state at 30 K, generates a double step transition with field on the magnetization (Fig. 3a) and spin transition with a magnetic hysteresis for the HS fraction (Fig. 3b). Here also, we keep the general properties of symmetry: the magnetization $m(h)$ is anti-symmetric with respect to h (Fig. 3a) while $n_{HS}(h)$ is a symmetric curve (Fig. 3b). These features remain valid for other temperatures. In the next panels (Fig. 3c, d), the domain of stable (S) states is large around $m = 0$ as obtained in Fig. 3a, b where the LS state is favored. At any value of the field energy in the range (-160 K)−(160 K), at least two states among stable (S), unstable (U) and metastable (M) can be obtained (see Fig. 3a, b). Similar phenomena are depicted in panels (e) and (f), where the interval of h values where the LS domain is stale is reduced states, and that of the HS state becomes larger. One can conclude that, when going from the boundaries of the thermal hysteresis of Fig. 1 loop to the interior, it emerges that the number of solutions increases. In this case, when the temperature is increased, the LS phase becomes less stable than the HS phase. The stability domain of the HS phase appears larger than that of the LS phase. In Fig. 4, we summarize the magnetic field dependence of the corresponding free energies of the solutions obtained in Figs. 2 and 3. Thus, we see in Fig. 3a that for $T = 30$ K, where the two magnetic hysteresis are quite well separated, the LS diamagnetic state ($m = 0$, $n_{HS} = 0$) is stable only in the intermediate magnetic field region, $-80 < h < +80$. Below $h = -80$ and above $h = +80$, the stable phases correspond to that of the HS state with the respective values of the order parameters, ($m = -1$, $n_{HS} = 1$) and ($m = +1$, $n_{HS} = +1$); i.e. with reversed signs of the magnetization. According to this behavior, it is then remarked that the HS fraction exhibits a hysteresis behavior as function of the applied magnetic field.

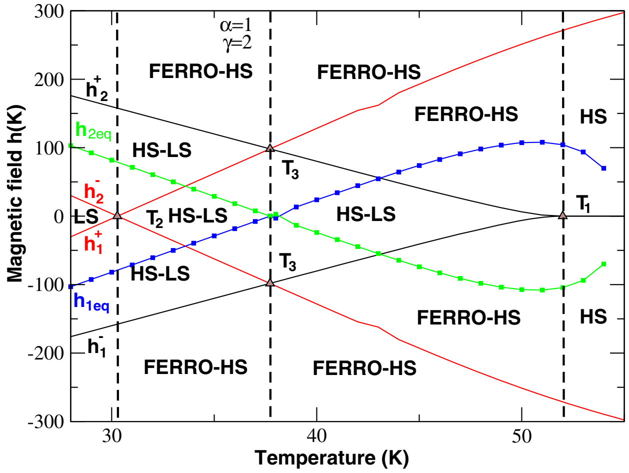

Fig. 5 Symmetric domains of stable S (HS and LS states) and metastable M (HS-LS) phases in $(T; h)$ plane for $\alpha = 1$ and $\gamma = 2$. For $T_1 = 52$ K, $h_1^- = h_2^+ = 0$ which is limited stable HS and HS-LS phases in high temperatures and for $T_2 = 30.27$ K, $h_1^+ = h_2^- = 0$, two phases are separated in HS-LS and LS stable phases. For $T_3 = 37.72$ K, separated phases HS-LS and HS are obtained at none zero magnetic-field energy and with its opposite values, whereas intermediate HS-LS phases prevail at zero field (see text). h_{1eq} and h_{2eq} are equilibrium fields obtained for $n_{HS} = 0.5$ with respect to the fields $h_1^\pm$ and $h_2^\pm$. For $T_3 = 37.72$ K, $h_{1eq} = h_{2eq} = 0$ in HS-LS phases

For $T = 35$ K, the h-dependence of the free energy (Fig. 4e) becomes complex, due to the interpenetration of the magnetic hysteresis, as seen in the curves of $m(h)$ and n_{HS}, depicted in Fig. 3c, d. There, we see for example that for $h = 0$, five (resp. three) solutions appear in $m(h)$ (resp. $n_{HS}(h)$) curves with the presence of horns in the free energy curves which enhance with the vanishing the intermediate stable LS sate.

A deep analysis of the static magnetic field effects, i.e. the h-dependence of the magnetization, m and the HS fraction n_{HS}, shows that the behavior of the isothermal quantities, $m(h)$ and $n_{HS}(h)$, crucially depend on temperature. That is because the output of the application of the magnetic field depends whether the considered temperature belongs in the considered thermal hysteresis to a bistable or a mono-stable phase (see Fig. 1c, d). Let's consider the case of Fig. 3 which presents and an interesting interplay between magnetic two h-induced magnetic and HS hysteresis. We consider the curves $m(h)$, on which we denote by $h_1^- < 0$ and $h_1^+ > 0$ (resp. $h_2^- < 0$ and $h_2^+ > 0$) the switching magnetic fields of the negative (resp. positive) part of the magnetization, respectively. We see clearly that these four spinodal fields, $h_1^\pm$ and $h_2^\pm$, are temperature-dependent, as clearly proved in the phase diagram of Fig. 5.

Thus, the case $T = 30$ K, shows two quite well-separated magnetic hysteresis (see Fig. 3a) for which the spinodal fields are so that $h_1^- < h_1^+ < h_2^- < h_2^+$. Below h_1^- the system is in the ferromagnetic HS state and above h_2^+ we recover again the HS state with a reversed magnetization. Here, the plateau is diamagnetic (LS) and consists in spins $\sigma = 0$. This case is characterized by a large plateau with a large stable phase and a single phase at $h = 0$.
At $T = 35$ K, the spinodal fields are such as $h_1^- < h_2^- < h_1^+ < h_2^+$. Therefore, the two magnetic hysteresis interfere, which reduces the width of stable phase for the benefit of the metastable (blue line) phase in the plateau region. In this situation, the system is no more mono-stable at $h = 0$ and the free energy $F(m, h = 0)$ depicts three wells, where the fundamental one is LS ($m = 0$) and the excited ones are metastable, with minimums obtained around $m = \pm 1$. Finally at $T = 40$ K, corresponding to the following relation between spinodal the fields, $h_2^- < h_1^- < h_2^+ < h_1^+$, the intermediate phase (corresponding to $m = 0$) becomes totally metastable and it is then expected that the free energy $F(m, h = 0)$ depicts again three wells, with two stable minimums around $m = \pm 1$ and another metastable minimum around $m = 0$.

Figure 5 summarizes the interplay between the HS and the LS phases as function of temperature. For that, we have drawn $h_1^\pm(T)$ and $h_2^\pm(T)$, delimiting the stability of the phases. From the LS to HS-LS states, the transition temperature in metastable M state is $T_2 = 30.27\,\mathrm{K}$ where the magnetic field vanishes, $h_1^+ = h_2^- = 0$, and in the HS state, $h_1^- = -h_2^+ = 157.8\,\mathrm{K}$. In the equilibrium state transition, HS-LS states are obtained from symmetric magnetic field $h_1^+ = h_2^+ = +98.2\,\mathrm{K}$ and $h_1^- = h_2^- = -98.2\,\mathrm{K}$ at $T_3 = 37.72\,\mathrm{K}$. By increasing the temperature to $T_1 = 52\,\mathrm{K}$, the fields $(h_2^+ = h_1^-)$ become zero again and beyond that, HS states take place. These phenomena become important where different states created under the influence of the field depend strongly on the temperature. Thus, equilibrium fields h_{1eq} and h_{2eq} are respectively, increasing function (blue curve) and decreasing function (green curve) of temperature, and at high temperature they disappear in HS domain where $n_{HS} \simeq 1$.

3.2 Nonequilibrium properties of the system inside the thermal hysteresis in zero-field energy

We turn to analyze the dynamical behavior of the system in the vicinity of the thermal hysteresis loop accompanying the thermally-induced first-order transition of (Fig. 1) on the magnetization m and HS fraction n_{HS}, by solving the equations of motion 13.

Figure 6 presents the time dependence of the magnetization and HS fraction along the relaxation from several initial states inside the thermal hysteresis of Fig. 1c, d at fixed temperature $T = 40$ K where the system exhibits a bistability at equilibrium on both magnetization, m and HS fraction, n_{HS} (see Fig. 1c, d). The nonequilibrium properties of the system reveal that the minimums (stable and metastable solutions) of the equilibrium the free energy functional are strong attractors. Indeed, the temporal evolution of the system, for the different initial values of m (from -1 to $+1$ with step 0.2) and n_{HS} (from 0 to 1 with step 0.25), reach the values $m = -1$ or $m = 0$ or $m = +1$ for the

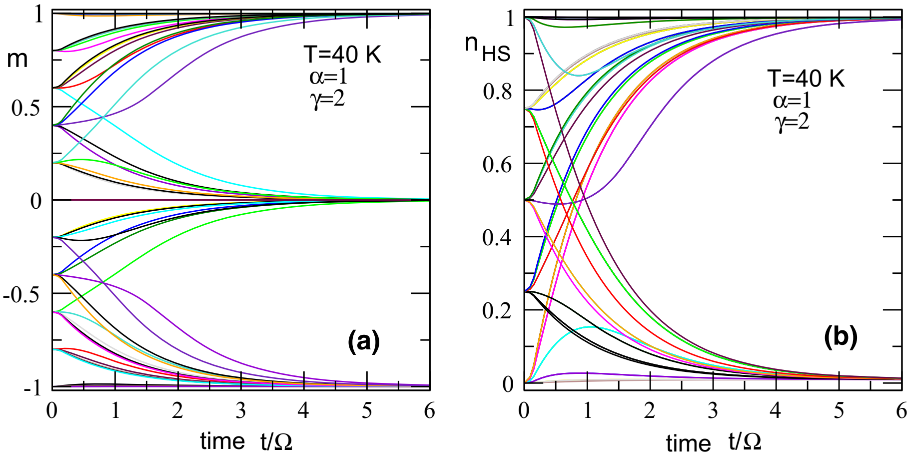

Fig. 6 Isothermal relaxation path of the magnetization m and HS fraction, n_{HS}, from several initial conditions on m and n_{HS}, towards their stable states. Within the corresponding thermal hysteresis loop, at $T = 40$ K and for $\alpha = 1$ and $\gamma = 2$, HS and LS are stable states obtained in the absence of magnetic-field energy. The simulations, were performed using the value, $\Omega = 2\pi$

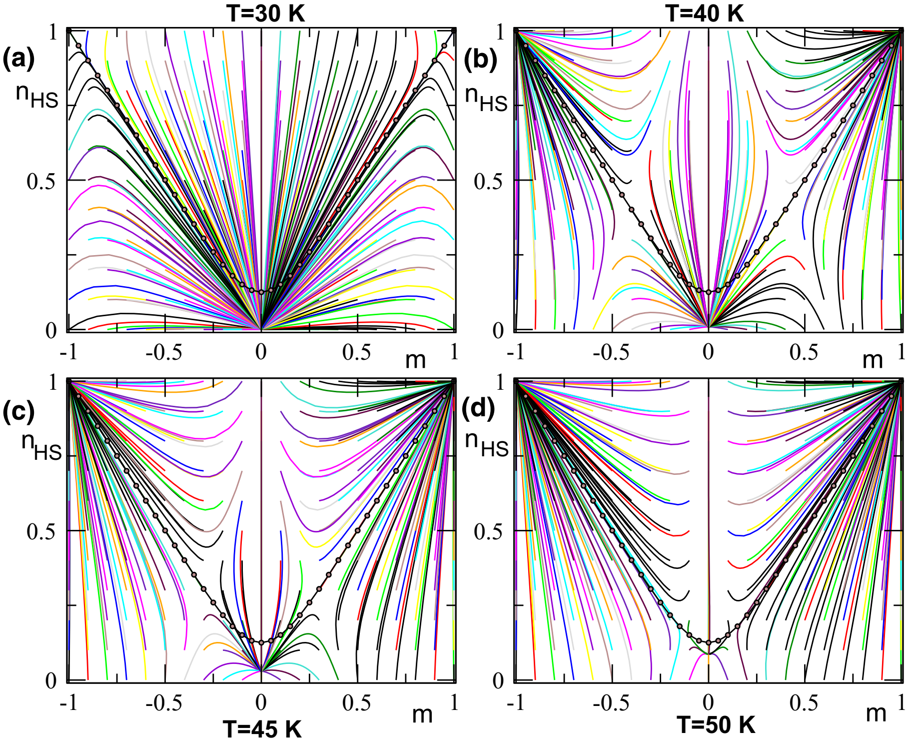

Fig. 7 Phases portrait of the model in (m, n_{HS}) plane at different temperatures for $\alpha = 1$ and $\gamma = 2$. According to Fig. 6, the relaxation path follows the limited equilibrium line which is expressed by Eq. (15). In Panel (a) $T = 30$ K, all curves converge to the attracted point which is in the LS state. In panels (b) and (c), $T = 40$ K and $T = 45$ K, respectively, HS and LS states are the attracted points within the corresponding thermal hysteresis loop (Fig.1). In panel (d), the stable states are almost in HS states that are obtained at $T = 50$ K, from which, more and more stable in high temperatures. Others parameters are $\alpha = 1$ and $\gamma = 2$

magnetization and $n_{HS} = 0$ (LS) or $n_{HS} = +1$ (HS) for the HS fraction, according to the initial states (see Fig. 6).

Thus, in panel (a), starting from any initial value between -1 and $+1$, the magnetization m evolves in time to one of the stable state -1, 0 or $+1$ according to the selected initial value of n_{HS}. Similar results are got in panel (b) where the time-dependence of the HS fraction strongly depends on the initial value of the magnetization at time $t = 0$. Panels a–d of Fig. 7 display the phase portraits or the flow diagrams of the system obtained in (m, n_{HS}) plane at different temperatures,

$T = 30, 40, 45, 50$ K, during its isothermal relaxation from several initial points in its phase space, formed by the variable m, n_{HS}. All data correspond to the situation of Fig. 1c, d.

At low temperature, $T = 30K$, where Fig. 1c, d show a single stable state (LS), the corresponding phase portrait (Fig. 7a) shows a unique attractor located at coordinates ($m = 0$, $n_{HS} = 0$) to which converge all the $n_{HS}, (m)$ curves whatever the values of the initial states, indicating the monostability of the system. In contrast, at $T = 40$ K, i.e. inside the bistability region of the thermal hysteresis, of Figs. 1 (panels c, d), 7b depicts three attractors, located at coordinates ($m = 0$, $n_{HS} = 0$) for the LS state and ($m = +1$, $n_{HS} = 1$) and ($m = -1$, $n_{HS} = 1$) for the HS state. When the temperature increases (see panels c and d), two states +1 and −1 (HS states) prevail in agreement with the thermal equilibrium data of Fig. 1c, d. In addition, all curves follow more or less the equilibrium path, represented by the dotted parabola of equation,

$$m = n_{HS} \tanh(\beta J z m), \tag{15}$$

obtained from the ratio of the equilibrium equations (14) in zero magnetic field. This equilibrium path represents a strong attractor to all system trajectories, particularly around the stationary states.

4 Conclusion

The bistability of magnetically-interacting spin-crossover solids is modeled by the Blume-Emery-Griffiths spin-1 model and investigated through the mean-field theory, in the presence of an external constraint represented by a magnetic field energy, influencing the system properties. The kinetic equations that describe the evolution of the system are derived from the microscopic master equation approach are solved in static and dynamic cases. In the static case, and at fixed temperature, multi-step transitions are obtained as function of the magnetic field, leading to phase transitions with magnetic hysteresis between ferromagnetic and diamagnetic (or HS and LS) states. The phase diagram of the system is studied in the plane (T, h) and the possible coexistence of different phases between the spinodal magnetic fields (boundaries of the hysteresis) has been elucidated. The nonequilibrium properties of the system have been also investigated at constant temperature inside and outside the thermal hysteresis regions for $h = 0$. It is revealed that the isothermal relaxation curves converge to the stationary states (stable points) of the system, following different trajectories depending on the initial values of the magnetization and the HS fraction. The analysis of the phase portrait of the system showed the existence of a local equilibrium path, which has the form of a "parabola" in the plane (m, n_{HS}) to which all the trajectories converge along the relaxation process. Overall, these results are interesting and open the way for relevant applications in the control of the spin-crossover from one hand and the magnetic state, from the other hand, by a magnetic field. Indeed, the magnetic field allows here the switching between diamagnetic and ferromagnetic states, which correspond to the LS and HS states, which have different elastic and mechanical properties. Among the possible extensions of this work, one may notice the investigations of the dynamical properties using a radio-frequency magnetic field which will produce limiting cycles and nonlinear effects which will be revealed thanks to the two-step transitions of the order parameters under magnetic field.

Acknowledgements The authors would like to thank J. Linares for fruitful discussions on the present results. T.D. OKE acknowledges financial support from the "Groupe d'Etudes de la Matière Condensée" (GEMaC) of the "Université de Versailles Saint-Quentin" (UVSQ) and CNRS during a visit.

Data Availability Statement This manuscript has no associated data or the data will not be deposited. [Authors' comment: The generated data are obtained with Fortran Code based on evolving system equations and help us to display all figures reported in this paper which are available on request by T. D. OKE.]

References

1. P. Gütlich, H.A. *Goodwin, Spin-crossover in transition metal compounds I , II and III*, vol. 233–235 (Berlin, Springer, 2004)
2. J.H. Ammeter, Nov. J. Chem. **4**, 631 (1980)
3. S. Ohkoshi, K. Hashimoto, J. Am. Chem. Soc. **121**, 10591 (1999)
4. S. Ohkoshi, S. Ikeda, T. Hozumi, T. Kashiwagi, K. Hashimoto, J. Am. Chem. Soc. **128**, 5320 (2006)
5. S. Ohkoshi, K. Imoto, Y. Tsunobuchi, S. Takano, H. Tokoro, Nat. Chem. **3**, 564 (2011)
6. P. Gütlich, A. Hauser, H. Spiering, Angew. Chem. Int. Ed. **33**, 2024 (1994)
7. J.M. Herrera, V. Marvand, M. Verdager, J. Marrot, M. Kalisz, C. Mathoniere, Angew. Chem. Int. Ed. **43**, 5468 (2004)
8. N. Nègre, C. Conséjo, M. Goiran, A. Bousseksou, F. Varret, J.P. Tuchagues, R. Barbaste, S. Askénazy, J.G. Haasnoot, Phys. B **294–295**, 91 (2001)
9. H. Tokoro, S.-I. Ohkoshi, K. Hashimoto, Appl. Phys. Lett. **82**, 1245 (2003)
10. F. Varret, K. Boukheddaden, C. Chong, A. Goujon, B. Gillon, J. Jeftic, A. Hausser, Eur. Phys. Lett. **77**, 30007 (2007)
11. D.A. Pejakovíc, J.L. Mauson, C. Kitamura, J.S. Miller, A.J. Epstein, Polyhedron **20**, 1435 (2001)
12. K. Kato, Y. Moritomo, M. Takata, M. Sakata, M. Umekawa, N. Hamada, S. Ohkoshi, H. Tokoro, K. Hashimoto, Phys. Lett. **91**, 255502 (2003)
13. H. Banerjee, S. Chakraborty, T. Saha-Dasgupta, Inorganics **5**, 47 (2017)
14. A. Gîndulescu, A. Rotaru, J. Linares, M. Dimian, J. Naser, J. Phys. Conf. Ser. **268**, 012007 (2011)

15. M. Nishino, S. Miyashita, P.A. Rikvold, Phys. Rev. B **96**, 144425 (2017)
16. C. Enashescu, L. Stoleriu, A. Stancu, A. Hausser, Phys. Rev. B **82**, 104114 (2010)
17. M. Sorai, S. Seki, J. Phys. Chem. Solids **35**, 555 (1974)
18. M.M. Dîrtu, C. Neuhausen, A.D. Naik, A. Rotaru, L. Spinu, Y. Garcia, Inorg. Chem. **49**, 5723 (2010)
19. W. Nicolazzi, J. Pavlik, S. Bedoui, G. Molnár, A. Bousseksou, Eur. Phys. J. Spec. Topics **222**, 1137 (2013)
20. M. Paez-Espejo, M. Sy, K. Boukheddaden, J. Am. Chem. Soc. **138**, 3202 (2016)
21. M.A. Halcrow, *Spin-Crossover Materials: Properties and Applications* (Wiley, New York, 2013)
22. P. Gütlich, A.B. Gasper, Y. Garcia, Beilstein J. Org. Chem. **9**, 342 (2013)
23. C.M. Quintero, G. Félix, I. Suleimanov, J.S. Costa, G. Molnár, L. Salmon, W. Nicolazzi, A. Bousseksou, Beilstein J. Nanotechnol. **5**, 2230 (2014)
24. E. König, Struct. Bond. **76**, 51 (1991)
25. H. Spiering, N. Willenbacher, J. Phys. Condens. Matter **1**, 10089 (1989)
26. Y. Ogawa, A. Mino, S. Keshihara, K. Koshino, T. Ogawa, C. Urano, H. Takagi, Phys. Rev. lett. **84**, 3181 (2000)
27. K. Boukheddaden, J. Linares, H. Spiering, F. Varret, Eur. Phys. J. B **15**, 317 (2000)
28. K. Boukheddaden, I. Shteto, B. Hôo, F. Varret, Phys. Rev. B **62**, 14796 (2000)
29. K. Boukheddaden, I. Shteto, B. Hôo, F. Varret, Phys. Rev. B **62**, 14806 (2000)
30. M. Nishino, S. Miyashita, Phys. Rev. B **63**, 174404 (2001)
31. M. Nishino, K. Boukheddaden, S. Miyashita, F. Varret, Phys. Rev. B **72**, 064452 (2005)
32. K. Boukheddaden, M. Nishino, S. Miyashita, F. Varret, Phys. Rev. B **72**, 014467 (2005)
33. H. Watanabe, N. Bréfuel, S. Mouri, J.-P. Tuchagues, E. Collet, and Tanaka. Eur. Phys. Lett. **96**, 17004 (2011)
34. K. Boukheddaden, M. Sy, M. Paez-Espejo, A. Slimani, F. Varret, Phys. B **486**, 187 (2016)
35. M. Paez-Espejo, M. Sy, F. Varret, K. Boukheddaden, Phys. Rev. B **89**, 024306 (2014)
36. C. Chong, F. Varret, K. Boukheddaden, Phys. Rev. B **81**, 014104 (2010)
37. C. Enachescu, R. Tanasa, A. Stancu, F. Varret, J. Linares, E. Codjovi, Phys. Rev. B **72**, 054413 (2005)
38. M. Sy, D. Garrot, A. Slimani, M. Paez-Espejo, F. Varret, K. Boukheddaden, Angew. Chem. **55**, 1755 (2016)
39. K. Boukheddaden, Eur. J. Inorg. Chem. (2014). https://doi.org/10.1002/ejic.201201093
40. B. Hôo, K. Boukheddaden, F. Varret, Eur. Phys. J. B **17**, 449 (2000)
41. A. Slimani, F. Varret, K. Boukheddaden, D. Garrot, H. Oubouchou, S. Kaizaki, Phys. Rev. Lett. **110**, 087208 (2013)
42. H. Romstedt, A. Hauser, H. Spiering, J. Phys. Chem. Solids **59**, 265 (1998)
43. K. Boukheddaden, F. Varret, S. Salinke, J. Linares, E. Codjovi, Phase Trans. **75**, 733 (2002)
44. M. Paez-Espejo, M. Sy, F. Varret, K. Boukheddaden, Phys. Rev. **89**, 024306 (2014)
45. S. Mouri, K. Tanaka, S. Bonhommeau, N.O. Moussa, G. Molnár, A. Bousseksou, Phys. Rev. B **78**, 17308 (2008)
46. A. Bousseksou, J. Nasser, J. Linares, K. Boukheddaden, F. Varret, J. Phys. I **2**, 1381 (1992)
47. A. Bousseksou, F. Varret, J. Nasser, J. Phys. I **3**, 1463 (1993)
48. H. Bolvin, Chem. Phys. **211**, 101 (1996)
49. J. Pavlik, W. Nicolazzi, G. Molnár, R. Boča, A. Bousseksou, Eur. Phys. J. B **86**, 292, (2013)
50. I. Gudyma, V. Ivashko, J. Linares, J. Appl. Phys. **116**, 173509 (2014)
51. M. Nishino, S. Miyashita, K. Boukheddaden, J. Chem. Phys. **118**, 4594 (2003)
52. J. Wajnflasz, Phys. Status Solidi B **40**, 537 (1970)
53. J.A. Naser, Eur. Phys. J. B **21**, 3 (2001)
54. J.A. Nasser, S. Topçu, L. Chassagne, M. Wakim, B. Bennali, J. Linares, Y. Alayli, Eur. Phys. J. B **83**, 115 (2011)
55. A. Rotaru, A. Carmona, F. Combaud, J. Linares, A. Stancu, J. Nasser, Polyhedron **28**, 1684 (2009)
56. A. Rotaru, J. Linares, S. Mordelet, A. Stancu, J. Nasser, J. Appl. Phys. **106**, 043507 (2009)
57. J.A. Nasser, Eur. Phys. B **48**, 19 (2009)
58. A. Rotaru, J. Linares, E. Codjovi, J. Nasser, A. Stancu, J. Appl. Phys. **103**, 07B908 (2008)
59. A. Slimani, K. Boukheddaden, K. Yamashita, Phys. Rev. B **92**, 014111 (2015)
60. M. Nishino, S. Miyashita, Phys. Rev. B **88**, 014108 (2013)
61. K. Boukheddaden, M. Nishino, S. Miyashita, Phys. Rev. B **75**, 094112 (2007)
62. J.A. Nasser, K. Boukheddaden, J. Linares, Eur. Phys. J B **39**, 219 (2004)
63. T.D. Oke, F. Hontinfinde, K. Boukheddaden, Eur. Phys. J. B **86**, 271 (2013)
64. T.D. Oke, F. Hontinfinde, K. Boukheddaden, Appl. Phys. A **120**, 309 (2015)
65. T.D. Oke, F. Hontinfinde, K. Boukheddaden, Comput. Condens. Matter **9**, 27 (2016)
66. M. Nishino, K. Boukheddaden, S. Miyashita, F. Varret, Polyhedron **24**, 2852 (2005)
67. M. Nishino, K. Boukheddaden, S. Miyashita, F. Varret, Phys. Rev. B **68**, 224402 (2003) (**references therein**)
68. S.B. Ogou, T.D. Oke, F. Hontinfinde, K. Boukheddaden, Adv. Theory Simul. **2**, 1800192 (2019)
69. K. Boukheddaden, S. Miyashita, M. Nishino, Phys. Rev. Lett. **100**, 177206 (2008)
70. G. D'Avino, A. Painelli, K. Boukheddaden, Phys. Rev. B **84**, 104119 (2011)